

The vacuum melted γ -TiAl (Nb, Cr, Si)-doped alloys and their cyclic oxidation properties

M. N. Mathabathe ^{a,b*}, A.S. Bolokang^{a**}, G. Govender^a, R. J. Mostert^b, C.W. Siyasiya^b

^aCouncil of Scientific Industrial Research, Materials Science and Manufacturing, Light Metals, Meiring Naude Road, P O Box 395 Pretoria, South Africa

^bDepartment of Material Science and Metallurgical Engineering, Faculty of Engineering, Built Environment and Information Technology, University of Pretoria, South Africa

Abstract

The γ -TiAl intermetallic alloy doped with Nb, Cr, and Si metals has been developed. It has emerged that the ternary Ti-48Al-2Nb and quinary Ti-48Al-2Nb-0.7Cr-0.3Si alloys yielded the best mechanical and cyclic oxidation properties. In particular, the quinary Ti-48Al-2Nb-0.7Cr-0.3Si alloy rapidly developed the protective stable Al₂O₃ oxide doped with nitrogen and titanium oxynitride during cyclic oxidation. This showed a lower hardness when compared to the other alloys after cyclic oxidation. The oxide layer proved to have a good adhesive relationship with the parent metal. The alloys microstructures were analysed with the scanning electron microscopy (SEM). The sample hardness test were conducted by Vickers hardness tester.

Keywords: Ti-48Al-2Nb-0.7Cr-0.3Si alloy; Ti-48Al-2Nb alloy; Vacuum melted; cyclic oxidation; oxynitrides;

* Corresponding Author: Ms. Maria Mathabathe, Tel: (+27) 12 841 7224

Email: nmathabathe@csir.co.za

** Corresponding Author: Dr. Amogelang Bolokang, Tel: (+27) 12 841 3295,

Email: sbolokang@csir.co.za

Research Highlights

- Ti-48Al, Ti-48Al-2Nb, Ti-48Al-2Nb-0.7Cr and Ti-48Al-2Nb-0.7Cr-0.3Si were developed.
- Ti-48Al-2Nb and Ti-48Al-2Nb-0.7Cr-0.3Si has excellent mechanical properties
- Ti-48Al-2Nb and Ti-48Al-2Nb-0.7Cr-0.3Si revealed best cyclic oxidation resistance.
- Formation of oxynitrides mixed with $\text{Al}_2\text{O}_3/\text{TiO}_2$ was detected.

1. Introduction

Titanium (Ti) and its alloys are the preferred materials for aerospace, medical, and nuclear field because of their attractive properties such as light weight but high strength as well as corrosion resistance. These alloys encounter challenges due to rapid gaseous corrosion at high application temperatures. The Ti-based alloys with emphasis on γ -TiAl intermetallic alloys are potential candidate for many high-temperature structural applications. It is one of the most important research material for scientists and engineers aiming to minimise the effect of both oxidation and oxygen embrittlement when these materials are in applications. One of the γ -TiAl intermetallic competitive material for high temperature applications are NiAl alloys [1-3]. Different approaches have been adopted to resolve the high temperature oxidation, leading to the development of coatings to prevent detrimental environmental effect on these alloys [4-6]. The heat and creep-resistant intermetallic substrates deposited with nanocrystalline γ -TiAl intermetallic TiAl-based coatings micro-alloyed with Cr atoms induced very good oxidation resistance at 1173 K [4]. Furthermore, $\text{TiAl}_3/\text{Al}_2\text{O}_3$ composite powders were prepared by high energy ball milling and subsequent heat-treatment. The $\text{TiAl}_3/\text{Al}_2\text{O}_3$ powders deposited on γ -TiAl intermetallic and decreased the oxidation rate of γ -TiAl substrate [7] and Cr_2AlC coatings with better Al rich oxide scale [8]. The laser aided manufacturing of γ/β - Al_2O_3 coating on NiCrAlY coatings proved to withstand the operating temperature of 1200°C for ten cycles [9]. Additionally, another method of improving the properties of γ -TiAl alloys is to modify their chemical composition with alloying elements. For example, doping of traditional high temperature alloys such as β -NiAl to improve cyclic oxidation have been investigated [10-12]. Also, attempts to improve the oxidation resistance of Ti-Al intermetallic phase based alloys showed positive results [13-17]. Ding et al, [18] further investigated Nb-doped TiAl for cyclic deformation and microstructure evolution of high Nb containing TiAl alloy during high temperature low cycle fatigue. Our current investigation focus on the innovative alloying elements to produce the binary, ternary, quaternary and quinary alloys by addition of the Nb, Cr and Si γ -Ti-Al alloys. The arc button melting performed under vacuum was employed to manufacture the four γ -TiAl based alloys of nominal composition binary Ti-48Al (at. %), ternary Ti-48Al-2Nb (at.%), quaternary Ti-48Al-2Nb-0.7Cr (at.%) and quinary

alloys. The purpose for this research is to analyse the properties of these alloys and their oxidation resistance in air at 900 °C for 9 cycles of 900 hours (h).

2. Experimental procedures

2.1 Alloy preparation

The alloys were prepared by blending and cold pressing pure metallic powders Ti, Al, Nb, Cr, and Si with the mean particles sizes of 30, 74, 24, 126 and 9 μm , respectively. The alloy powder was blended for 3 hours in a tubular mixer, with subsequent uniaxial cold pressing at 380 MPa to produce cylindrical compacts of 43 mm diameter. The materials (γ -TiAl based alloys) examined in this study had a nominal composition Ti-48Al, Ti-48Al-2Nb, Ti-48Al-2Nb-0.7Cr, Ti-48Al-2Nb-0.7Cr-0.3Si (at. %). Finally the powder compacted alloys were melted under vacuum of 1×10^{-5} Torr using electric arc melting furnace, for heating. The arc is protected using a non-consumable tungsten electrode. The protective argon atmosphere ensures an oxygen free chamber which prevents oxidation of the alloy material during heating.

2.2 Materials characterization

Metallographic preparation was carried out using conventional techniques. Specimen surfaces were prepared for microstructural analysis under the scanning electron microscope (SEM) by grounding to a mirror-like surface using grit papers up to 4000 followed by 1 μm alumina, colloidal silica and then etched in 24ml H_2O + 50ml glycerol + 24ml HNO_3 + 2ml HF. The SEM is a JEOL® JSM-6510 instrument model which was conducted in a back scattered electron (BSE) mode equipped with energy dispersive X-ray spectroscopy (EDS) capabilities for micro-analysis. The analysis position of the energy-dispersive spectrometer (EDS) had a working distance (WD) of 10mm and a take-off angle of 35° for x-ray signals, which make possible efficient analysis and low-magnification mapping analysis under the same conditions as high-resolution secondary electron imaging (SEI) observation. For example, resolution of 3.0nm is guaranteed, and at low accelerating voltages it realises 8nm at 3.0kV and 15nm at 1kV. Moreover, the EDS, an energy-dispersive X-ray analyser is provided with a high-performance PTTD (position and time tagged data) function, whose digital electronics makes rapid high-precision analysis with minimal error as possible. The average grain size was determined by employing the line intercept method. The structural development was done with X-ray diffraction (XRD) using $\text{CuK}\alpha$ radiation $\lambda=1.54062 \text{ \AA}$ and 2θ from 20° - 90° angles. Image analysis was carried out to determine the size and volume fraction of the phase constituents using image j and digimizer software's; the measurements were carried out based on a minimum of

Vickers hardness measurements were performed on machined specimens (in the as-sintered and oxidized conditions). The macro-hardness was 20Kgf with dwelling time was 15 seconds for the test. Specimens were ground and polished using 1 μ m diamond suspension, followed by final polishing using 50 nm colloidal silica.

2.3 Hardness measurements

In order to perform hardness measurements, machined specimens (in the as-sintered and oxidized conditions) were ground and polished using 1 μ m diamond suspension, followed by final polishing using 50 nm colloidal silica, as outlined in ASTM standard E3-11. Vickers hardness tests were performed according to the requirements of ASTM standards E384-11. An applied load of 20Kgf and a dwelling time of 10 seconds were employed for the macro-hardness measurements. Hardness profiles throughout the specimens were measured at 0.2 mm intervals and average of at-least 15 measurements

2.4 Tensile test

Flat tensile specimens of 5mm \times 3mm cross-section and 12mm gauge length were prepared for room temperature tensile tests. The specimens were machined from the centre of the as-cast ingot button by electrical discharge machining. To prevent crack initiation, the tensile specimen were ground along the gauge length in longitudinal direction with SiC grit paper in water. The dimensions of the tensile specimens are shown in Fig.1. The uniaxial tensile test was conducted at room temperature using a MTS criterion C45 tensile machine at a constant crosshead speed of 0.25mm/min. Three tests were performed for each condition and average values were taken.

2.5 Cyclic oxidation

The cyclic oxidation test was conducted at 900 $^{\circ}$ C in a static laboratory air up to a maximum of 9 cycles. Each cycle consisted of exposure for 100 hours at test temperature and 15 mins at ambient temperature, which was sufficient to cool the specimens below 50 $^{\circ}$ C. The specimens were enclosed into and removed from the hot zone of the furnace within few seconds. Changes in mass of the specimens were recorded after each thermal cycle. However, prior the oxidation test, specimens used

in the test were homogenised at 1100 °C for one hour, followed by polishing up to 600 grit SiC papers, and ultrasonically cleaned with acetone for 20 minutes to remove any organic substances. The oxidised specimen surfaces were ground up to 1200 SiC grit papers in order to conduct metallographic examination. The morphology of the scale and specimen cross-section were investigated by SEM, and micro-analysis were performed by EDS.

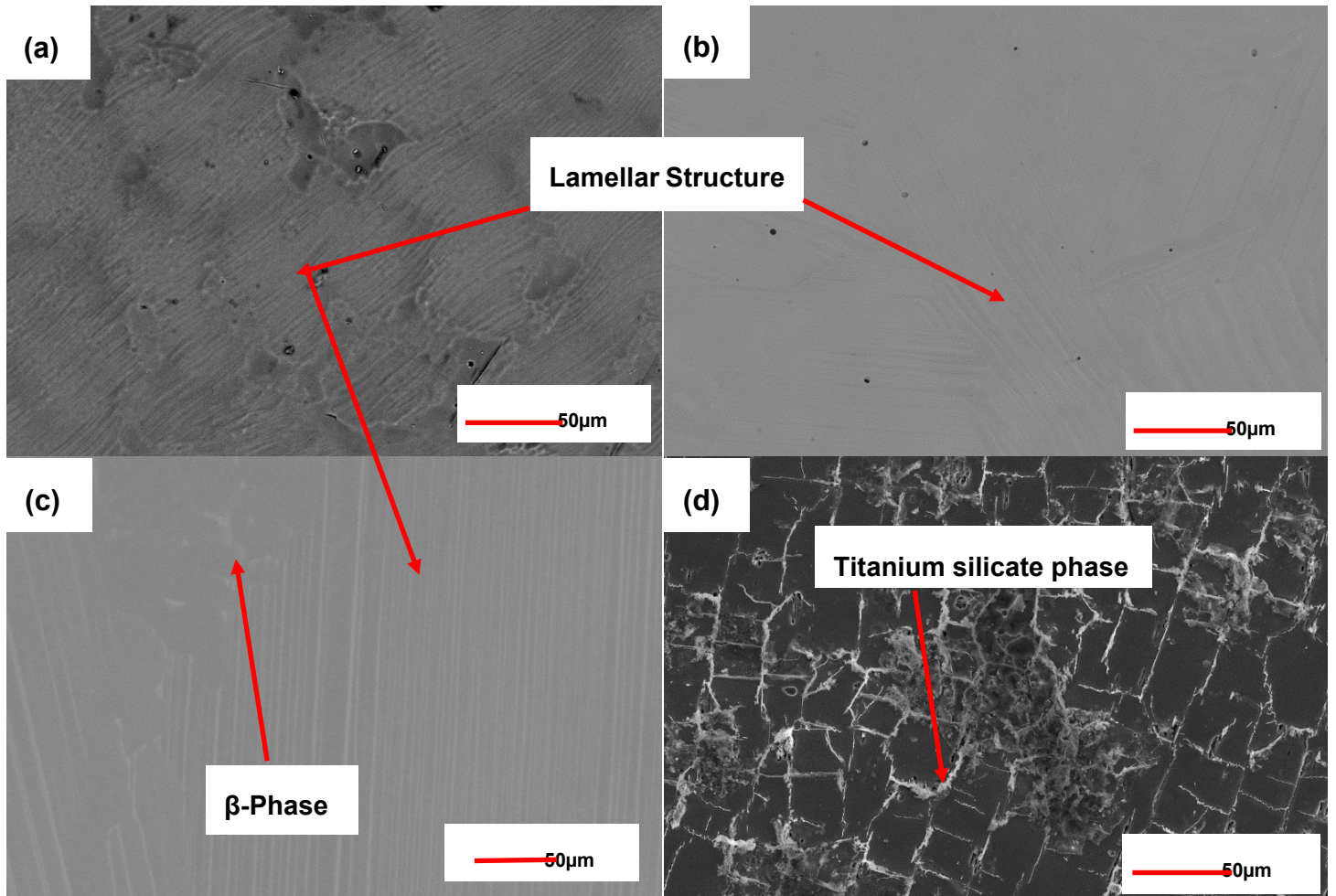


Fig. 1: The SEM micrographs of (a) Ti-48Al, (b) Ti-48Al-2Nb, (c) Ti-48Al-2Nb-0.7Cr and (d) Ti-48Al-2Nb-0.7Cr-0.3Si alloys

3. Results and Discussion

3.1 Analysis of the structure and properties of the as-melted four alloys

Fig. 1: The SEM micrographs of (a) binary (Ti-48Al), (b) ternary (Ti-48Al-2Nb), (c) quaternary (Ti-48Al-2Nb-0.7Cr) and (d) quinary (Ti-48Al-2Nb-0.7Cr-0.3Si) alloys

Fig. 1a-d shows the SEM images of the Ti-48Al, Ti-48Al-2Nb, Ti-48Al-2Nb-0.7Cr, Ti-48Al-2Nb-0.7Cr-0.3Si alloys, respectively. The multi-phase structures and the solute segregation were observed in the investigated γ -TiAl based alloys, which contributes to the mechanical properties of their corresponding alloys. The microstructures of the three alloys; Ti-48Al, Ti-48Al-2Nb, Ti-48Al-2Nb-0.7Cr all comprised of the \square -TiAl lamellae structure. The addition of Nb to the TiAl alloy modify the solidification behaviour of binary TiAl alloy system. Liu et al, [19] reported that partial alloying with Nb in Ti-48Al-2Nb improves the melting point nearly 100 °C and promote β -phase zone shifting to the high Al direction, inducing the multi-phase structure ($\alpha_2\gamma$ lamellar, B2 phase) while the scatter microstructure distribution indeterminate the TiAlNb alloy design for the favourable mechanical properties [20]. As shown in **Fig 1b**, the ternary alloy display evidence of elongated ordered β -phase in the inter-dendritic regions of the structure. Furthermore, the quinary microstructure (**Fig. 1d**) reveals a block-layered structures. The chemical analysis of the four γ -TiAl based alloys synthesised by vacuum arc button melting showing both nominal and actual chemical analysis is shown in **Table 1**. After vacuum melting the chemical analysis varied with the starting nominal composition according to thermodynamic feasibility reactions of the elements.

Fig. 2: The macro-hardness and grain size of Ti-48Al, Ti-48Al-2Nb, Ti-48Al-2Nb- 0.7Cr, Ti-48Al-2Nb-0.7Cr-0.3Si alloys

Fig. 2 shows the relationship between the Vickers macro-hardness and respective grain sizes of the Ti-48Al, Ti-48Al-2Nb, Ti-48Al-2Nb-0.7Cr, Ti-48Al-2Nb-0.7Cr-0.3Si alloys. The Ti-48Al alloy has grain size of 280 μm with the lowest hardness value of

Table 1: Chemical composition (at.%) of Ti-48Al, Ti-48Al-2Nb, Ti-48Al-2Nb-0.7Cr, Ti-48Al-2Nb-0.7Cr-0.3Si alloys

Alloys	Nominal composition (at. %)					As-vacuum melted alloy composition (at. %)				
	Ti	Al	Nb	Cr	Si	Ti	Al	Nb	Cr	Si
Binary	52	48				55.7	44.3			
Ternary	50	48	2			52.38	45.82	1.8		
Quaternary	49.3	48	2	0.7		51.04	46.41	1.89	0.7	
Quinary	49	48	2	0.7	0.3	51.61	45.55	1.92	0.73	0.27

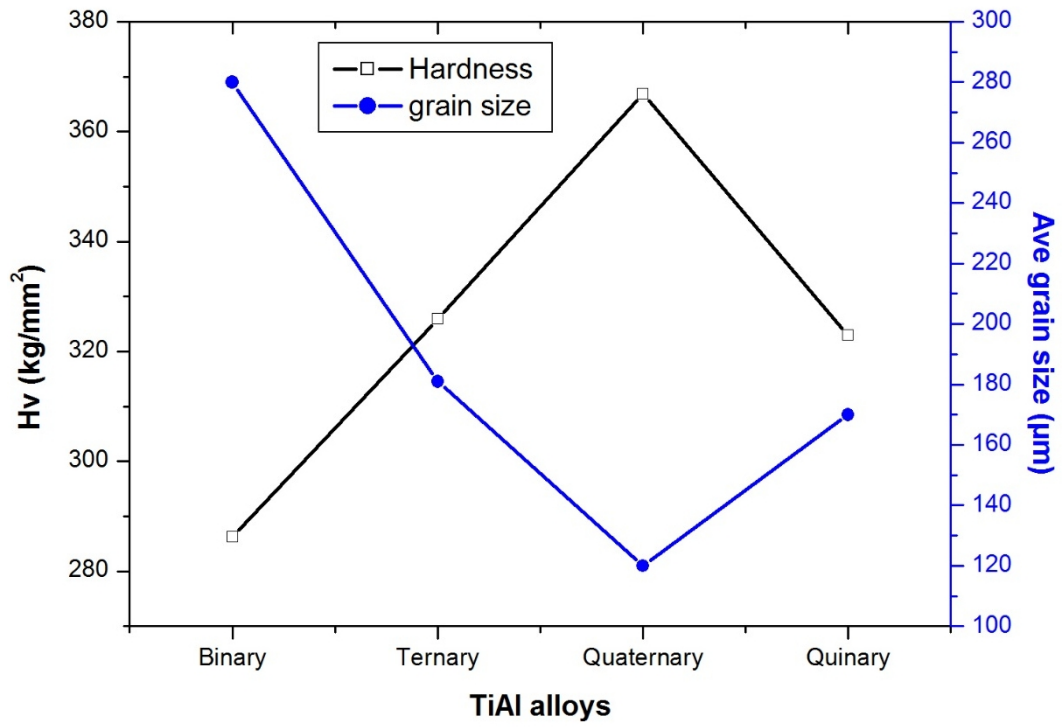


Fig. 2: The macro-hardness and grain size of the Ti-48Al, Ti-48Al-2Nb, Ti-48Al-2Nb-0.7Cr, Ti-48Al-2Nb-0.7Cr-0.3Si alloys

286 HV. Addition of Nb in TiAl reduced the grain size to 180 μm and increased hardness to 326 HV. Furthermore, Ti-48Al-2Nb-0.7Cr alloy shows the smallest grain size of 120 μm and hardness of 368 HV. Therefore, the combinational effect of Nb and Cr on γ -TiAl alloy acted as grain refiners. Alloying with Nb and Cr induced solid solution strengthening elements as well as beta stabilizing effect. Our results shows that Nb and Cr reduces the grain size of the TiAl alloy. The as-cast quaternary alloy microstructure is composed of ($\alpha_2\gamma$) lamellar structure and brittle isolated B2 phase shown in Fig. 1c. Furthermore, according to Liu et al, [19], the hardness values have a linear relationship with the yield stress in solidified TiAl alloys reflecting the material properties. The finer the grain size leads to high hardness, high strength and poor ductility. In the case of Ti-48Al-2Nb-0.7Cr-0.3Si, addition of Si has resulted in the slight increase of the grain size to 170 μm with hardness of 323 HV which may implicate that the ductility of the alloy was improved. **Fig. 3** follows the Hall Petch relationship in equation 1.

$$\sigma_y = \sigma_o + Kd^{-1/2} \quad (1)$$

σ_y is yield strength for permanent deformation of the material, σ_o and k are constants for the alloy and d is average diameter of the grains. Therefore, the smaller the grain size the higher the yield strength. Moreover, the presence of second phase titanium silicate (Ti_5Si_3) precipitated along the grain boundaries of the quinary alloy. This Ti-48Al-2Nb-0.7Cr-0.3Si quinary chemical combination alloy yielded the ultrafine lamellar spacing. The presence of Si promoted particle strengthening [21].

Fig. 3: Room temperature tensile test for the Ti-48Al, Ti-48Al-2Nb, Ti-48Al-2Nb-0.7Cr, Ti-48Al-2Nb-0.7Cr-0.3Si alloys based alloys

Fig. 3 shows the true stress vs. true strain curve, the comparison of the Ti-48Al, Ti-48Al-2Nb, Ti-48Al-2Nb-0.7Cr, Ti-48Al-2Nb-0.7Cr-0.3Si alloys. It is evident that Ti-48Al-2Nb-0.7Cr-0.3Si alloy has greater UTS, area under the graph and greater percentage elongation, compared to other alloys. This behaviour is attributed to the addition of Si in the TiAl based alloy since it enhances the room temperature ductility as a result of Ti_5Si_3 whiskers formation during solidification process [22]. The presence strip/rod-like Ti_5Si_3 phases in the microstructure may retard the motion of dislocations, leading to the improvement of strength [23]. Furthermore, Ti-48Al-2Nb-0.7Cr alloy

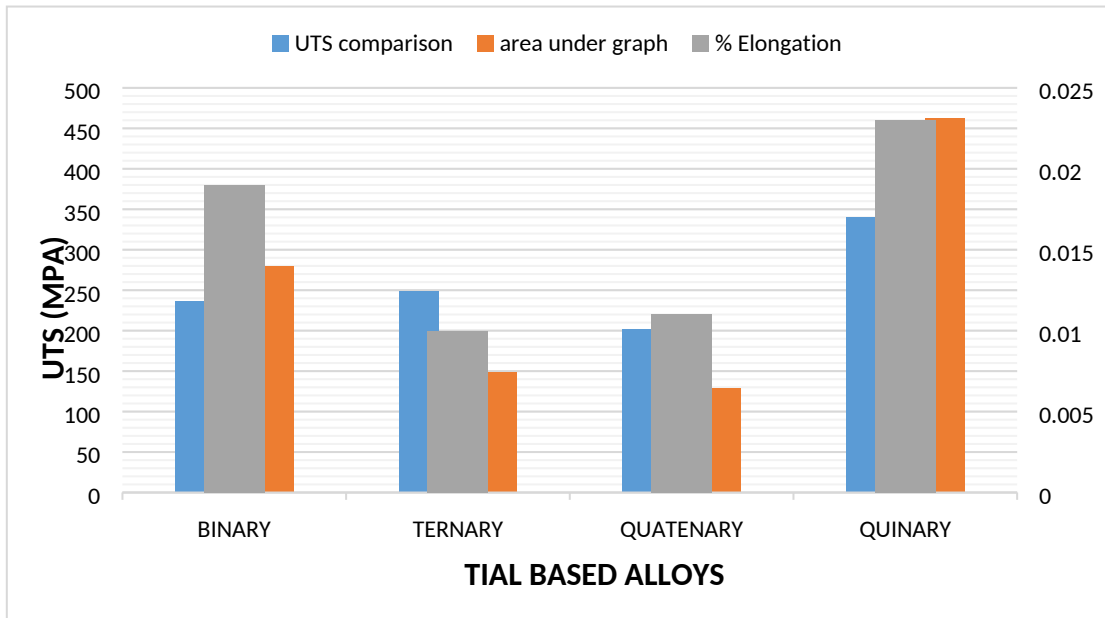


Fig. 3: Room temperature tensile test for the Ti-48Al, Ti-48Al-2Nb, Ti-48Al-2Nb-0.7Cr, Ti-48Al-2Nb-0.7Cr-0.3Si alloys

exhibits the lowest UTS when compared to the other alloys because of an intrinsic behaviour of Cr. The twin and super-dislocation nucleation are competing mechanisms in γ -TiAl alloys, depending on stacking fault energy [24]. When Cr atoms occupy Ti-sites in a single γ -phase alloy, it result in slight Ti-Al bond modification and plasticity enhancement [24]. In contrast, when Cr atoms occupy the Al sites in a duplex alloy, the overall covalence of Ti-Al bond is reduced and as a result favours plastic deformation which may seem to be the reason behind the lower UTS in the quaternary alloy [24]. Furthermore, a good combination of room temperature strength, ductility, toughness and creep strength can be attained when the lamellar boundaries are aligned parallel to the tensile direction [25].

3.2 Cyclic oxidation analysis of Ti-48Al, Ti-48Al-2Nb, Ti-48Al-2Nb-0.7Cr and Ti-48Al-2Nb-0.7Cr-0.3Si alloys

Fig. 4: Cyclic oxidation performed at 900 °C for 900 h on the Ti-48Al, Ti-48Al-2Nb, Ti- 48Al-2Nb-0.7Cr and Ti-48Al-2Nb-0.7Cr-0.3Si alloys

Fig. 4 shows the cyclic oxidation results of the Ti-48Al, Ti-48Al-2Nb, Ti-48Al-2Nb-0.7Cr, Ti-48Al-2Nb-0.7Cr-0.3Si alloys. Due to oxidation, the four alloys initially showed a sharp initial negative mass change during the first cycle (100 h). The significant mass loss experienced in all alloys initially may be an indication of oxide spallation on the sample surface, within the first 200 cycles. Upon longer exposure times, erratic specimen weight gain on the binary alloy was observed which became stable between 800 and 900 h. The binary alloy showed rapid formation of the oxide scale. After the seven cycles, a significant mass/weight loss associated with spallation and oxide regrowth has emerged. On the Ti-48Al-2Nb alloy there was no measurable mass loss found. Although the Ti-48Al-2Nb-0.7Cr alloy was stable from 200-900 h, a large negative mass change was recorded from 100-200 h exposure time. Furthermore, the Ti-48Al-2Nb-0.7Cr-0.3Si alloy resembled the Ti-48Al-2Nb alloy, since both showed resistance to cyclic oxidation than the Ti-48Al and Ti-48Al-2Nb-0.7Cr alloys. Addition of 2 at.% Nb to γ -TiAl intermetallic alloys improved oxidation resistance and inhibited oxide growth at high temperatures through enhanced adherence of the oxide scale

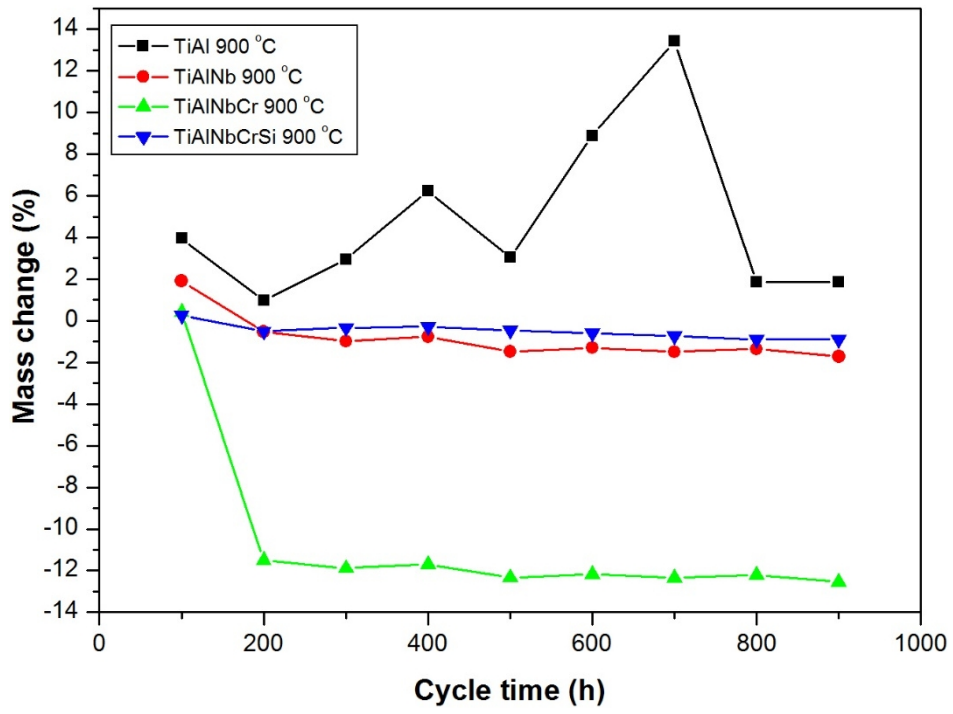


Fig. 4: Cyclic oxidation of Ti-48Al, Ti-48Al-2Nb, Ti-48Al-2Nb-0.7Cr, Ti-48Al-2Nb-0.7Cr-0.3Si alloys after cyclic oxidation

Furthermore, the Ti-48Al-2Nb-0.7Cr-0.3Si alloy illustrated the best performance compared to all the alloys, its percentage mass change was negligible throughout the 900 h exposure time. It has indicated a slight reduction in mass change and remained constant until the end of 900 h cycle. Although air is comprised of large quantity of nitrogen, Ti and Al has high affinity to O than N. However, N occupy O vacancies taking advantage of instability caused by vibrations at high temperature on oxides to form titanium oxynitride ($TiO_{2-x}N_x$). The oxynitrides layer formation reduced further oxygen diffusion into the surface.

Fig. 5: Surface oxides formed on (a) Ti-48Al, (b) Ti-48Al-2Nb, (c) Ti-48Al-2Nb-0.7Cr, (d) Ti-48Al-2Nb-0.7Cr-0.3Si alloys

Fig. 5 shows the SEM micrographs of the oxide layers formed on the surface of the Ti-48Al, Ti-48Al-2Nb, Ti-48Al-2Nb-0.7Cr, Ti-48Al-2Nb-0.7Cr-0.3Si alloys, respectively. In **Fig. 5a**, a prismatic crystalline powder illustrating smooth and irregular thin long Al_2O_3 particles was observed. This is in agreement with the severe cyclic oxidation observed on the Ti-48Al alloy shown in **Fig. 4**. The Ti-48Al-2Nb alloy in **Fig. 5b** scale show agglomeration of small particles attributable to the formation of mixed oxide on the ternary alloy surface. **Fig. 5c-d** resembled similar mixed oxide particles morphology and orientation.

Fig. 6: SEM images of Al_2O_3 scale obtained from Ti-48Al-2Nb, (c) Ti-48Al-2Nb-0.7Cr, (d) Ti-48Al-2Nb-0.7Cr-0.3Si alloys

The Al_2O_3 particles found on Ti-48Al-2Nb, (c) Ti-48Al-2Nb-0.7Cr, (d) Ti-48Al-2Nb-0.7Cr-0.3Si alloys oxide scales are illustrated in **Fig. 6**. The oxide SEM images of the Ti-48Al-2Nb (**Fig. 6b**) shows network of interconnected irregular particles. Additionally, the Ti-48Al-2Nb-0.7Cr formed Al_2O_3 particles are very porous, spider web type shape with features of the oxide found in Ti-48Al-2Nb alloy. **Fig. 6c** shows the Al_2O_3 particles obtained from Ti-48Al-2Nb-0.7Cr-0.3Si alloy after oxidation. The morphology of the scale is different from those of Ti-48Al-2Nb and Ti-48Al-2Nb-0.7Cr

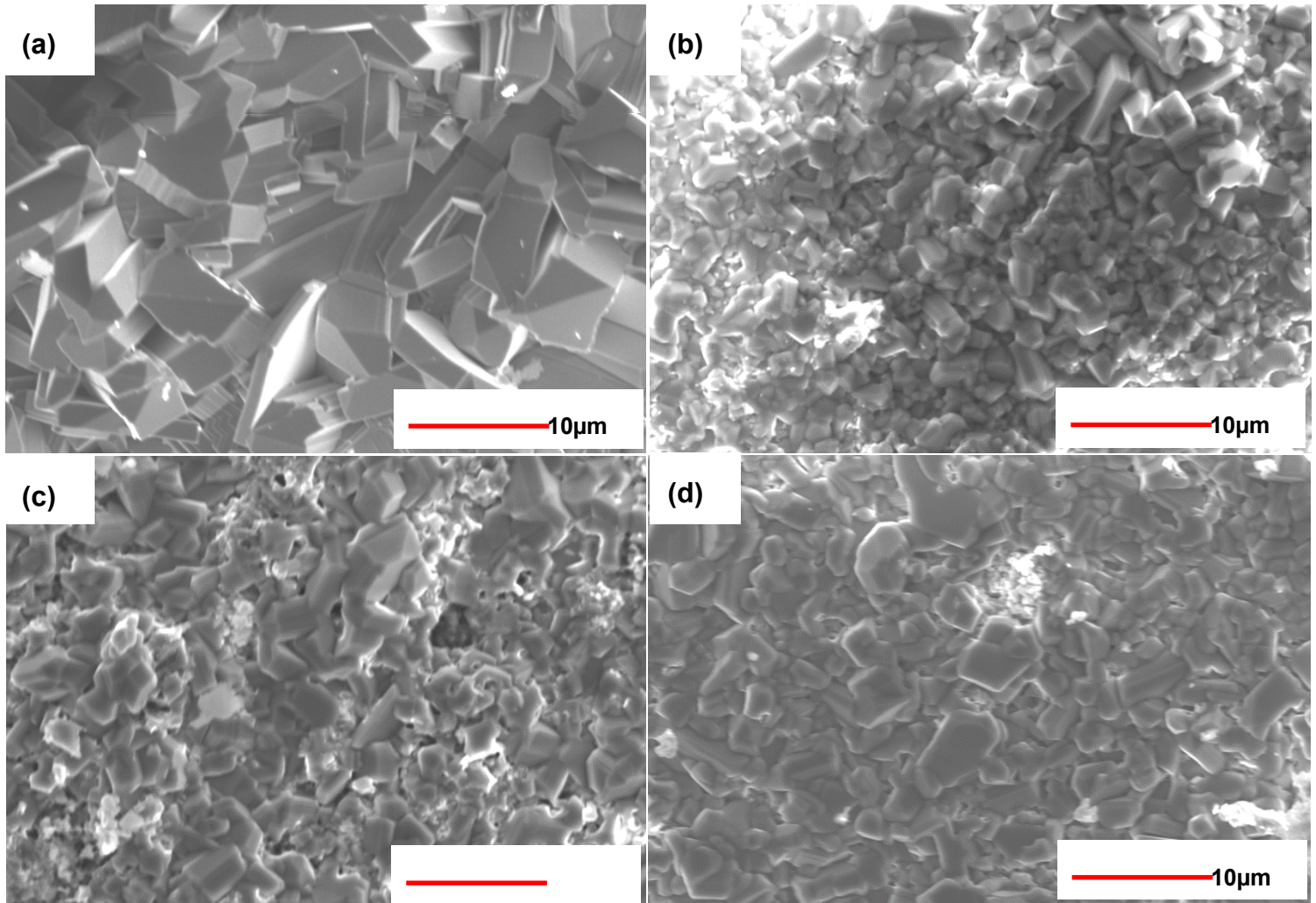


Fig. 5: Surface oxides formed on (a) Ti-48Al, (b) Ti-48Al-2Nb, (c)Ti-48Al-2Nb-0.7Cr and (d) Ti-48Al-2Nb-0.7Cr-0.3Si alloys

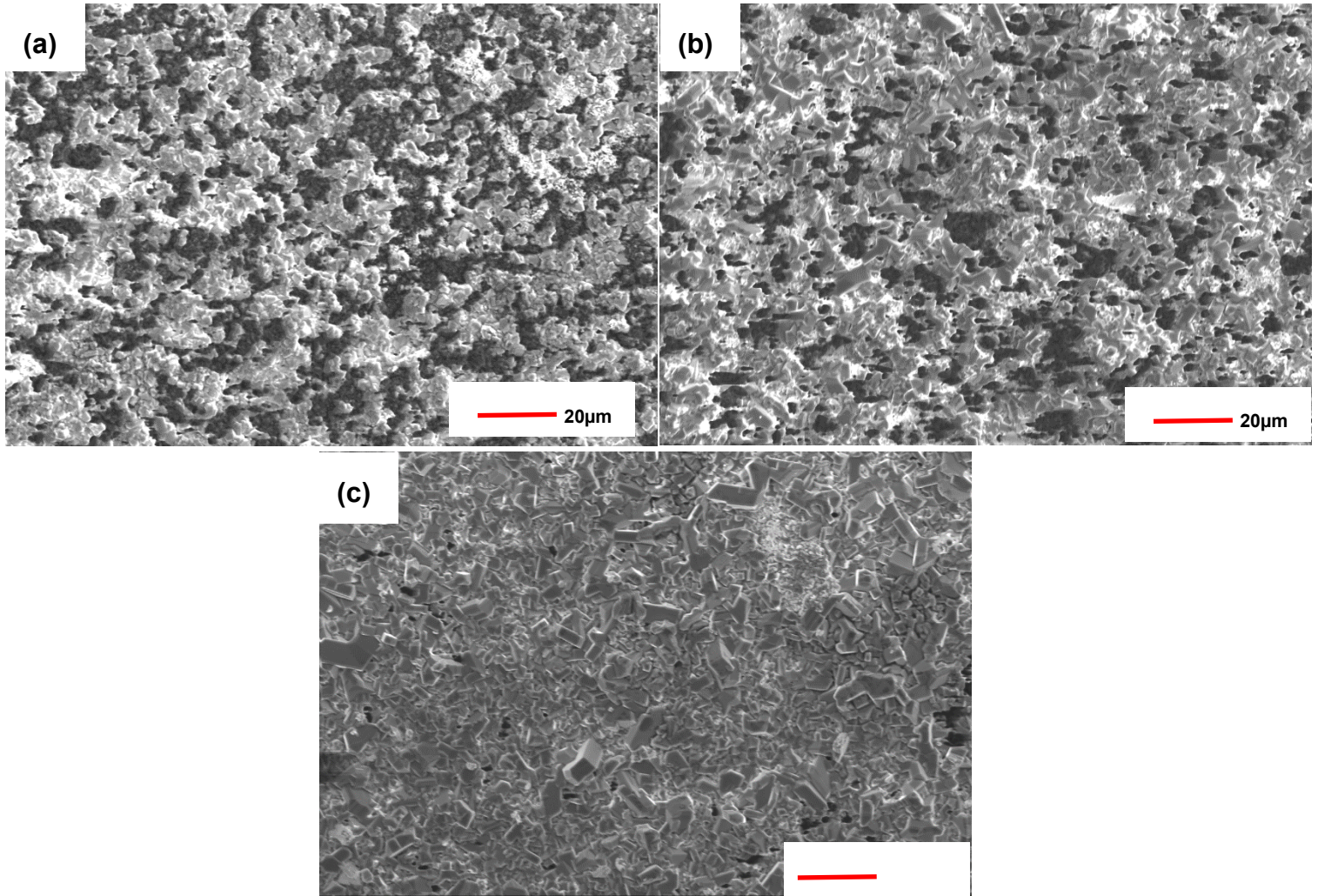


Fig. 6: SEM images of Al_2O_3 scale obtained from Ti-48Al-2Nb, (c) Ti-48Al-2Nb-0.7Cr, (d) Ti-48Al-2Nb-0.7Cr-0.3Si alloys

oxides, respectively. The particles are interconnected, non-porous and shows agglomeration but irregular in shape attributed to nitrogen content in Al_2O_3 with improved corrosion resistance [27].

3.3 Analysis and characterization of the oxide layers

Fig. 7: SEM images of the transverse sectioned (a) Ti-48Al, (b) Ti-48Al-2Nb, (c) Ti-48Al-2Nb-0.7Cr, (d) Ti-48Al-2Nb-0.7Cr-0.3Si alloys

Fig.7 shows a cross-sectional micrographs of the four alloys subjected to cyclic oxidation with the BSE scale images (Inset). EDS micro-analysis revealed in **Fig.8** shows that the primary constituents oxides dominating are alumina and titanium oxide/oxynitrides across the alloys. The binary TiAl alloy is comprised of rutile TiO_2 scale on the surface as shown in **Fig. 7a**. The layer display the alternating light and dark phases due the presence of nitrogen mainly enclosed in the core. The oxide showed poor adhesive behaviour to the parent metal as confirmed by the chipping of the scale shown in the BSE contrast inset image. In **Fig 7b** the alternating oxide layers is more adhesive due to Nb presence on the surface of the parent metal influencing the diffusion process by decreasing the oxide scale. The oxide scale comprised of mixed $\text{TiO}_2 + \text{Al}_2\text{O}_3$ layers formed on the alloy surface. Surprisingly, the chemical composition of the scale showed no significant amount of nitrogen. The initial stage of cyclic oxidation promoted Al-rich oxide scale to function as diffusion barrier by resisting the incoming oxygen, and effectively protected the parent metal from further oxidation. Furthermore, the alloy comprised with large crystalline grains on the surface of the parent metal making a clear boundary between the lamellar structure and enlarged grains. **Fig. 7b** shows the SEM microstructure of oxidized Ti-48Al-2Nb-0.7Cr alloy. The alloy oxide scale is comprised of mixed $\text{TiO}_2 + \text{Al}_2\text{O}_3$ with nitrogen impurities. The scale shows oxide surface chipping, peeling and fragile as shown in the BSE inset image. The initial scale formation dominated by TiO_2 layer and alternate with Al_2O_3 at the parent metal oxide phase boundary. The oxides penetrated the alloy at weaker grain boundaries. In the case of the Ti-48Al-2Nb-0.7Cr-0.3Si alloy shown in **Fig. 7d** it has the best cyclic oxidation performance. The oxide showed good adhesive properties to the parent metal throughout the cyclic oxidation period. Despite the

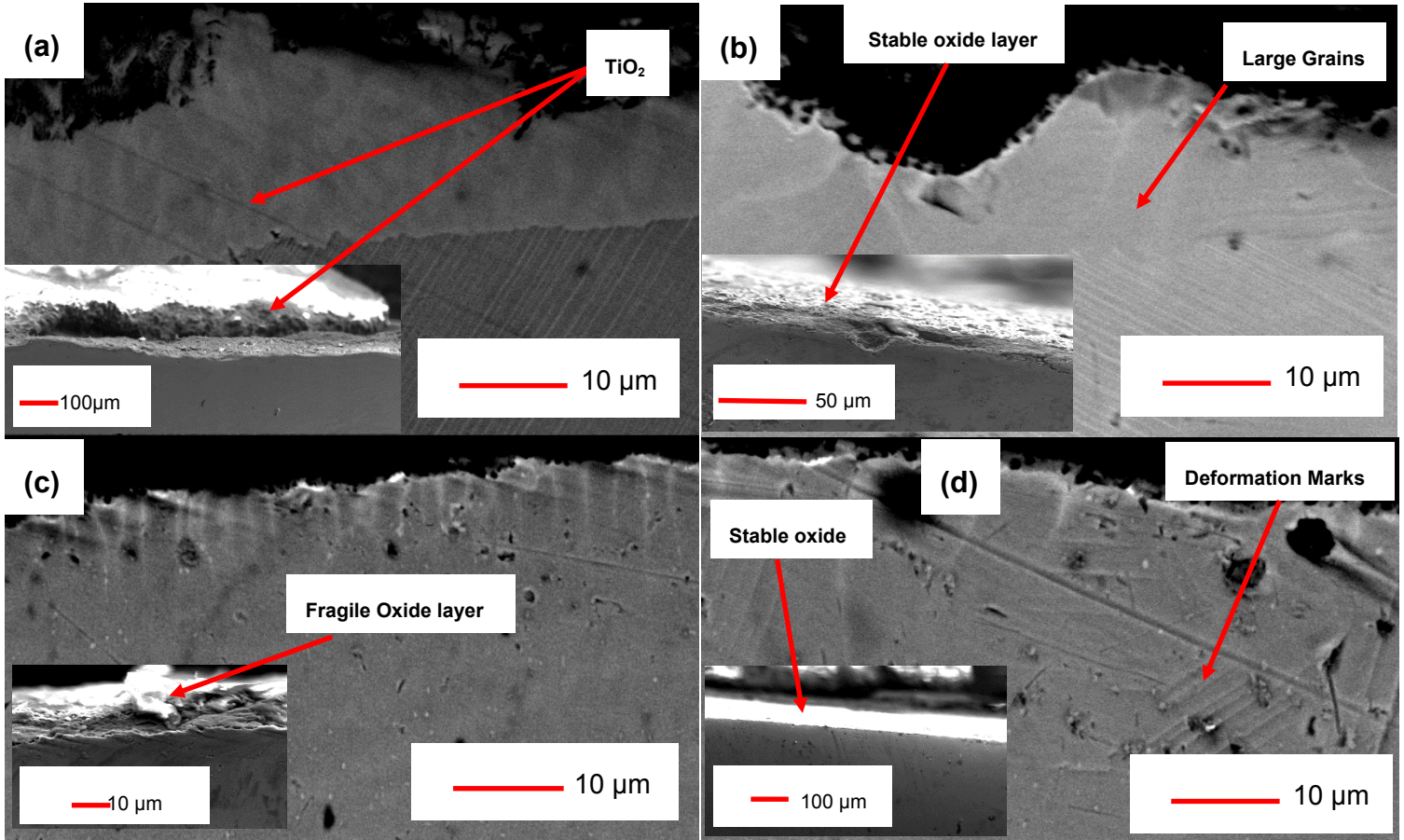


Fig. 7: SEM images of the transverse sectioned (a) Ti-48Al, (b) Ti-48Al-2Nb, (c) Ti-48Al-2Nb-0.7Cr and (d) Ti-48Al-2Nb-0.7Cr-0.3Si alloys

performance of quinary and the ternary alloy, the quinary alloy attest to its structural integrity by showing no major effect on the microstructure or any observed grain growth. Interestingly, the deformation marks were observed close to the alloy surface which are attributed to strain or compressive stresses induced by the oxynitride layer favouring the resistance to scale cracking due to mixed oxide/oxynitride structure [28]. Furthermore, the alumina scale exclusively grows by inward oxygen transport, appearing flat and adherent since the new oxide is formed nearly exclusively at the metal/oxide interface [28]. In the current study, the quinary alloy showed a low oxide growth due to the effect of Nb in the diffusion process by decreasing metal/oxygen transport [28] and the ability to form the oxynitride scale.

Fig. 8: EDS analysis of the oxides formed on the (a) Ti-48Al, (b) Ti-48Al-2Nb, (c) Ti- 48Al-2Nb-0.7Cr, (d) Ti-48Al-2Nb-0.7Cr-0.3Si alloys

The EDS analysis was performed on the oxide scales. Since the cyclic oxidation experiment was performed in air, it is logical to consider nitrogen contamination. **Fig. 8 a-d** displays the SEM images of the surface oxides with their corresponding EDS chemical composition. The binary alloy shown in **Fig. 8a** resemble a homogeneous oxide scale throughout the specimen attributed to TiO_2 with small amount of Al and N. The behaviour of oxidation and surface morphology on ternary and quaternary appear similar (**Fig. 8b-c**). However, the quaternary alloy illustrated relatively large spallation of oxide particles from the surface of the specimen compared to the ternary alloy probably due to the presence of Cr. On the other hand, the quinary alloy showed a homogeneous layer of oxide with some areas showing nodule-like pillar TiO_2 growth with the structure of the underlying substrate locally still noticeable. The varying compositions are indicated by the green, blue and black arrows in **Fig. 8d**. The white phases are comprised with low Al content similar to the composition of the binary alloy oxide scale. It is evident on the SEM micrographs of the γ -TiAl based alloys that the presence of Nb minimizes the formation of TiO_2 . Fraction of the scale in **Fig 8b-d** has slightly higher amount of Al content, confirming the formation of Al_2O_3 oxide layer.

The formation of Al_2O_3 (**equation 1**) is thermodynamically more feasible than the formation of TiO_2 (**equation 2**) at 900 °C. However, due to prolonged exposure in air γ -alumina phase absorbs the nitrogen ions to form a stable AlON non-stoichiometric compound rich of defect structures [29]. The formation of the oxynitride phases occur through oxygen substitution by nitrogen [30].

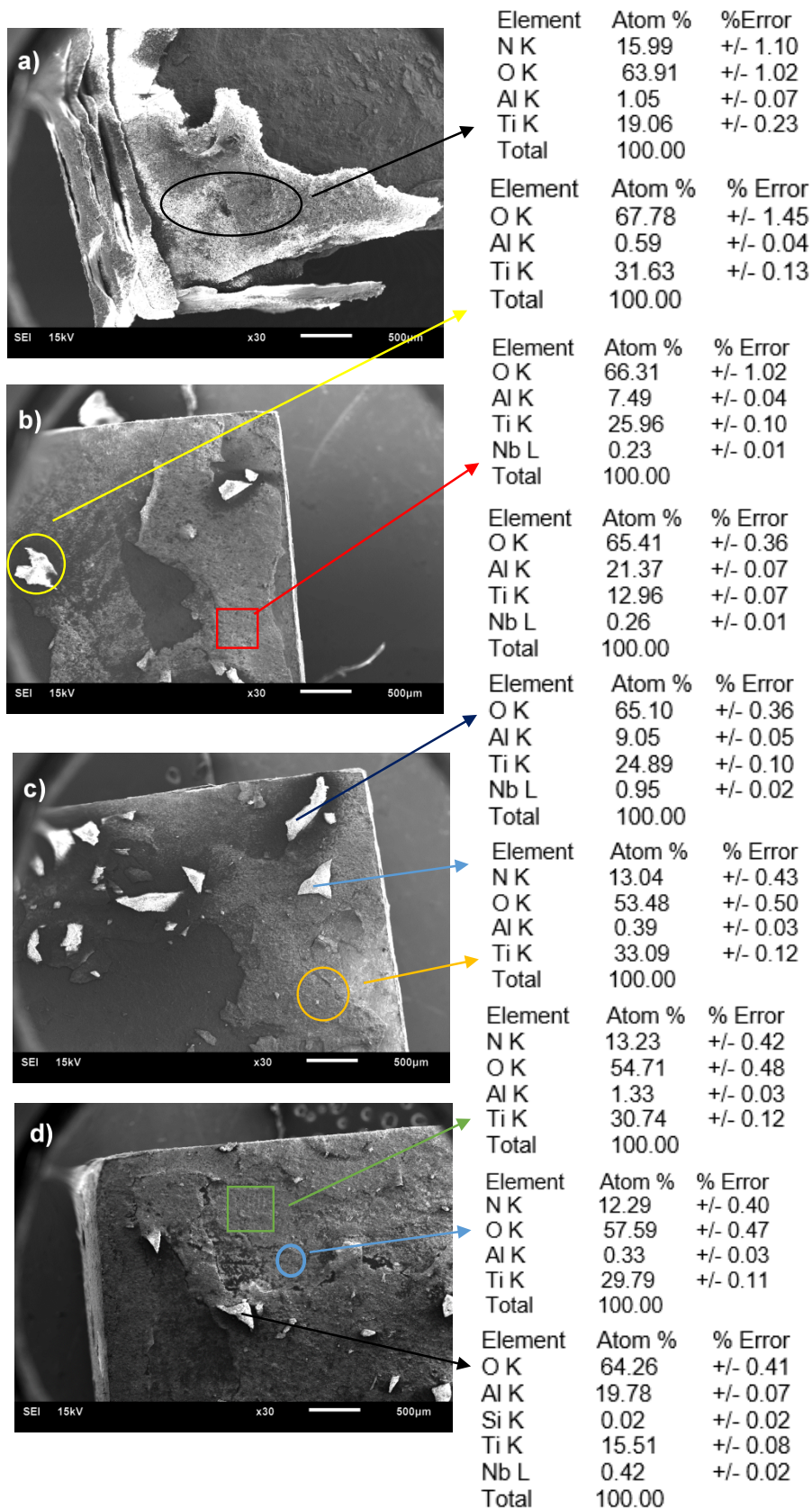


Fig. 8: EDS analysis of the oxides formed on the (a) Ti-48Al, (b) Ti-48Al-2Nb, (c) Ti-48Al-2Nb-0.7Cr and (d) Ti-48Al-2Nb-0.7Cr-0.3Si alloys

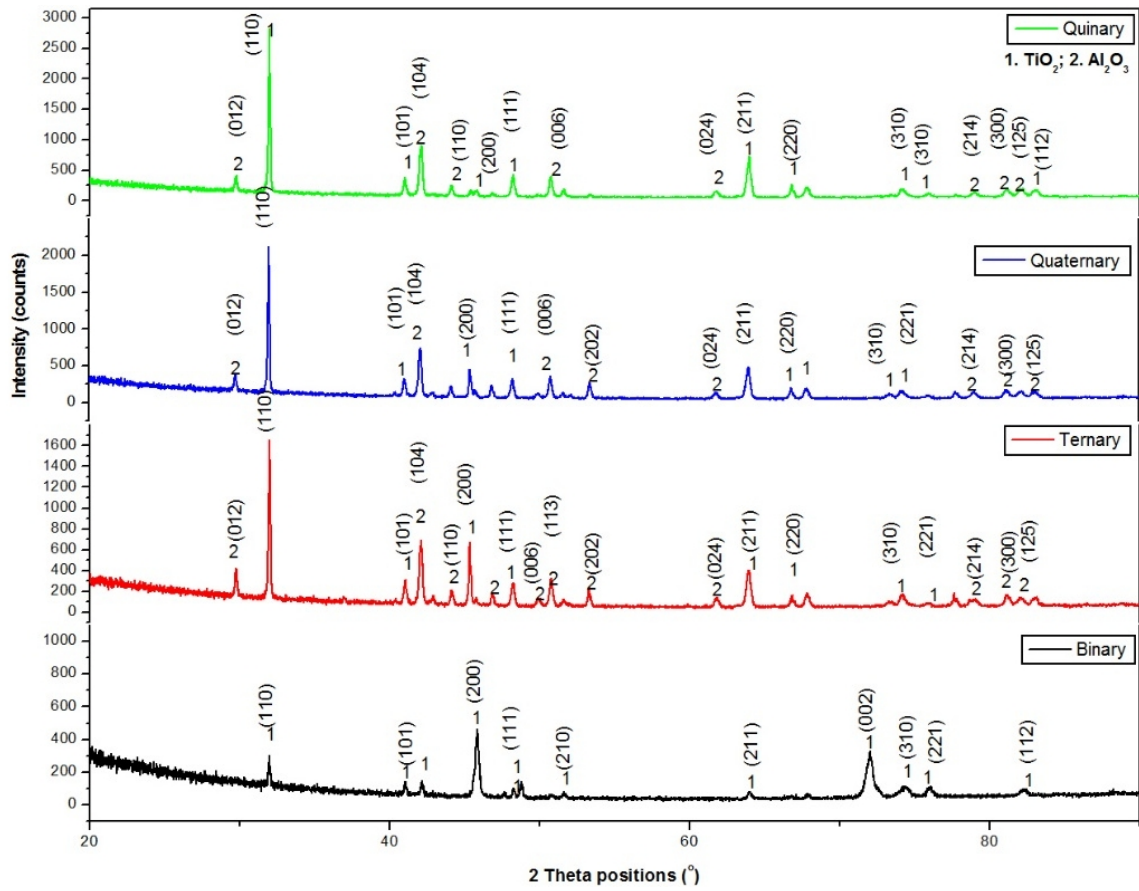


Fig. 9: XRD pattern of the cyclic oxidation oxides formed on Ti-48Al, Ti-48Al-2Nb, Ti-48Al-2Nb-0.7Cr, Ti-48Al-2Nb-0.7Cr-0.3Si alloys

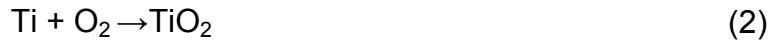


Fig. 9: XRD pattern of the cyclic oxidation oxides formed on Ti-48Al, Ti-48Al-2Nb, Ti-48Al-2Nb-0.7Cr, Ti-48Al-2Nb-0.7Cr-0.3Si alloys

The structural analysis of the oxides formed during cyclic oxidation of Ti-48Al, Ti-48Al-2Nb, Ti-48Al-2Nb-0.7Cr, Ti-48Al-2Nb-0.7Cr-0.3Si alloys is shown in **Fig. 9**. The XRD analysis confirms the formation of two dominant oxides TiO_2 and Al_2O_3 , respectively. Both oxide types were detected on the Ti-48Al-2Nb, Ti-48Al-2Nb-0.7Cr, and Ti-48Al-2Nb-0.7Cr-0.3Si alloys with exception of the TiAl alloy. This findings are in agreement with the SEM-EDS analysis. The TiO_2 belongs to rutile with tetragonal crystal structure and lattice parameters of $a=4.593 \text{ \AA}$; $c=2.959 \text{ \AA}$. The Al_2O_3 has rhombohedral structure of $a=4.764 \text{ \AA}$; $c=12.997 \text{ \AA}$ lattice parameters. These structures belongs to both oxides and oxynitrides ($\text{TiO}_{2-x}\text{N}_x/\text{Al}_2\text{O}_{3-x}\text{N}_x$) phases due to the detected nitrogen content especially on the quaternary and quinary alloys.

3.4 Hardness properties after cyclic oxidation

Fig. 10: Macro-hardness of the Ti-48Al, Ti-48Al-2Nb, Ti-48Al-2Nb-0.7Cr, Ti-48Al-2Nb-0.7Cr-0.3Si alloys after oxidation

The macro-hardness of Ti-48Al, Ti-48Al-2Nb, Ti-48Al-2Nb-0.7Cr, Ti-48Al-2Nb-0.7Cr-0.3Si alloys after 900 h exposure at 900 °C was measured. **Fig. 10** shows drastic changes on Ti-48Al-2Nb, Ti-48Al-2Nb-0.7Cr, and Ti-48Al-2Nb-0.7Cr-0.3Si when compared to **Fig. 2** (macro-hardness curve before cyclic oxidation). The binary TiAl hardness decreased from 286 to 247 HV while Ti-48Al-2Nb hardness was also reduced from 326 to 262 HV. Additionally, the highest rapid reduction in hardness was observed in the Ti-48Al-2Nb-0.7Cr alloy from 368 HV to 247.5 HV. This behavior is attributed to the grain growth as well as the brittleness induced by adsorption of oxides on the surface matrix of the alloy. On contrary, the Ti-48Al-2Nb-0.7Cr-0.3Si alloy

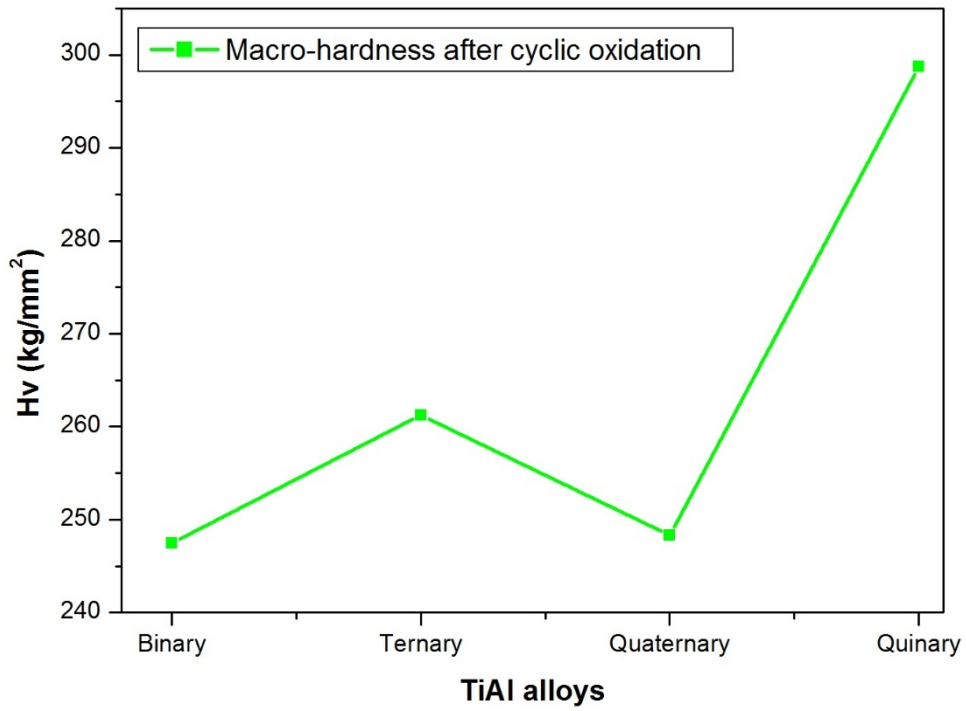


Fig. 10: Macro-hardness of the on Ti-48Al, Ti-48Al-2Nb, Ti-48Al-2Nb-0.7Cr, Ti-48Al-2Nb-0.7Cr-0.3Si alloys after cyclic oxidation

reduction was negligible from 323 HV to 298 HV after 900 h at 900 °C. The alloy showed the best performance compared to other alloys and this results are in agreement with cyclic oxidation results shown in **Fig. 4**.

4. Conclusion

The γ -TiAl based alloys with nominal composition Ti-48Al, Ti-48Al-2Nb, Ti-48Al-2Nb-0.7Cr and Ti-48Al-2Nb-0.7Cr-0.3Si were successfully synthesized by melting. These alloys were subjected to cyclic oxidation at 900 °C for 900 h and the conclusions of the investigation are as follows;

- 1) The Ti-48Al, Ti-48Al-2Nb, Ti-48Al-2Nb-0.7Cr and Ti-48Al-2Nb-0.7Cr-0.3Si were developed.
- 2) Both Ti-48Al-2Nb and Ti-48Al-2Nb-0.7Cr-0.3Si showed best mechanical properties and oxidation resistance when compared to Ti-48Al and Ti-48Al-2Nb-0.7Cr alloys.
- 3) Addition of Nb in Ti-48Al-2Nb promote β -phase zone inducing the multi-phase structure $\alpha_2\gamma$ lamellar, B2 phase while designed for the favourable mechanical properties. The properties are accompanied by reduced grain size from 280 HV to 180 μm and increased hardness from 280 to 326 HV.
- 4) The Ti-48Al-2Nb-0.7Cr-0.3Si alloy yielded the best properties of all alloys due to the presence of Ti_5Si_3 phase along the grain boundaries of the quinary alloy. The Ti-48Al-2Nb-0.7Cr-0.3Si alloy has grain size of 170 μm and hardness of 323 HV. This combination of hardness and grain size is attributed to the presence of second phase titanium silicate (Ti_5Si_3) precipitated along the grain boundaries and yielded the ultrafine lamellar spacing. The presence of Si promoted particle strengthening.
- 5) The Ti-48Al-2Nb-0.7Cr-0.3Si alloy has the highest tensile strength and % elongation. Furthermore, the alloy has the highest hardness after 900 h at 900 °C.
- 6) During fabrication processing of the alloys, under vacuum arc melting the solidification path of Si containing gamma-based TiAl quinary alloy, occurs in two stages viz.: First are randomly distributed large Ti_5Si_3 whiskers, formed by the solidification reaction $L \rightarrow \text{Ti}_5\text{Si}_3$ before the primary solidification $L1\beta \rightarrow$. The

second are the eutectic Ti_5Si_3 whiskers, formed by the eutectic reaction $L \rightarrow Ti_5Si_3$ between the dendrite arms after the primary solidification [24].

- 7) Due to oxide formation on the surface, the four alloys initially shows a sharp initial weight loss at the beginning of the oxidation during the first cycle. Subsequent to longer exposure times there was rapid mass increase on the binary alloy which became stable between 800 and 900 h. The binary alloy showed rapid formation of the oxide scale but after seven cycles significant mass loss was found which may be associated with spallation and oxide re-growth. Formation of oxynitrides mixed with Al_2O_3/TiO_2 favoured the Ti-48Al-2Nb-0.7Cr-0.3Si alloy.

5. Acknowledgement

Department of Science and Technology (DST) and Council of Scientific Industrial Research (CSIR) is acknowledged for funding this work. Finally, the technical support from the University of Pretoria and Mintek mainly for the provision of some of the laboratory equipment's.

6. References

- [1] D. Li, H. Guo, D. Wang, T. Zhang, S. Gong, H. Xu, Cyclic oxidation of β -NiAl with various reactive element dopants at 1200 °C, *Corros. Sci.* 66 (2013) 125–135.
- [2] C. Zhao, Y. Zhou, Z. Zoua, L. Luo, X. Zhao, F. Guoa, P. Xiao, Effect of alloyed Lu, Hf and Cr on the oxidation and spallation behavior of NiAl, *Corros. Sci.* 126 (2017) 334–343.
- [3] J. He, Y. Luan, H. Guo, H. Peng, Y. Zhang, T. Zhang, S. Gong, The role of Cr and Si in affecting high-temperature oxidation behaviour of minor Dy doped NiAl alloys, *Corros. Sci.* 77 (2013) 322–333.
- [4] B. Wendler, M. Danielewski, K. Przybylski, A. Rylski, Ł. Kaczmarek, M. Jachowicz, New type AlMo-, AlTi- or Si-based magnetron sputtered protective coatings on metallic substrates, *J. Mater. Proc. Technol.* 175 (2006) 427–432.
- [5] X. Gong, R. Chen, Q. Wang, Y. Wang, N. Zhang, Z. Zhang, H. Fu, Cyclic oxidation behavior and oxide scale adhesion of Al/NiCrAlY coating on pure titanium alloy, *J. Alloys Compd.* 729 (2017) 679–687.
- [6] D.J. Kim, D.Y. Seo, X. Huang, Q. Yang, Y.-W. Kim, Cyclic oxidation behavior of a beta gamma powder metallurgy TiAl–4Nb–3Mn alloy coated with a NiCrAlY coating, *Surf. Coat. Technol.* 206 (2012) 3048–3054.
- [7] J. Wang, L. Kong, T. Li, T. Xiong, A novel TiAl₃/Al₂O₃ composite coating on γ -TiAl alloy and evaluating the oxidation performance, *Appl. Surf. Sci.* 361 (2016) 90–94
- [8] Q.M. Wang, R. Mykhaylonka, A. Flores Renteria, J.L. Zhang, C. Leyens, K.H. Kim, Improving the high-temperature oxidation resistance of a β - γ TiAl alloy by a Cr₂AlC coating, *Corros. Sci.* (2010) 3793–3802.
- [9] M. Ansari, R. Shoja-Razavi, M. Barekat, H.C. Man, High-temperature oxidation behavior of laser-aided additively manufactured NiCrAlY coating, *Corros. Sci.* 118 (2017) 168–177.
- [10] D. Li, H. Guo, D. Wang, T. Zhang, S. Gong, H. Xu, Cyclic oxidation of β -NiAl with various reactive element dopants at 1200°C, *Corros. Sci.* (2013) 125–135.

- [11] H.B. Guo, Y.J. Cui, H. Peng, S.K. Gong, Improved cyclic oxidation resistance of electron beam physical vapor deposited nano-oxide dispersed β -NiAl coatings for Hf-containing superalloy, *Corros. Sci.* 52 (2010) 1440–1446.
- [12] J.A. Haynes, B.A. Pint, Y. Zhang, I.G. Wright, Comparison of the cyclic oxidation behavior of β -NiAl, β -NiPtAl and γ/γ' -NiPtAl coatings on various super alloys, *Surf. Coat. Technol.* 202 (2007) 730–734.
- [13] X. Liu, K. You, Z. Wang, M. Zhang, Z. He, Effect of Mo-alloyed layer on oxidation behavior of TiAl-based alloy, *Vacuum* 89 (2013) 209-214.
- [14] Z.Y. He, Z.X. Wang, X.P. Liu, P.D. Han, Preparation of TiAl-Cr surface alloy by plasma-surface alloying technique, *Vacuum* 89 (2013) 280-284.
- [15] N. Toshio, I. Takeshi, M. Yatagai, T. Yoshioka, Sulfidation processing and Cr addition to improve oxidation resistance of TiAl intermetallics in air at 1173 K, *Intermetallics* 8 (2000) 371-379
- [16] J. Malecka, W. Grzesik, A. Hernas, An investigation on oxidation wear mechanisms of Ti-46Al-7Nb-0.7Cr-0.1Si-0.2Ni intermetallic-based alloys, *Corros. Sci.* 52 (2010) 263-272.
- [17] Y. Shen, F. Wang., High temperature oxidation behaviour of Ti-Al-Nb ternary alloys, *J. Mater. Sci.* 39 (2004) 6583-6589.
- [18] J. Ding, Y. Liang, X. Xu, H. Yu, C.i Dong, J. Lin, Cyclic deformation and microstructure evolution of high Nb containing TiAl alloy during high temperature low cycle fatigue, *Int. J. Fatigue* 99 (2017) 68–77.
- [19] G. Liu, Z. Wang, T. Fu, Y. Li, H. Liu, T. Li, M. Gong, and G. Wang, Study on the microstructure, phase transition and hardness for the TiAl-Nb alloy design during directional solidification, *J. Alloys Compd.* 650 (2015) 45–52.
- [20] X. F. Ding, J. P. Lin, L. Q. Zhang, Y. Q. Su, H. L. Wang, and G. L. Chen, Lamellar orientation control in a Ti-46Al-5Nb alloy by directional solidification, *Scr. Mater.* 65 (1) (2011) 61–64.
- [21] E. Hamzah, M. Kanniah, and M. Harun, Effect of chromium addition on microstructure, tensile properties and creep resistance of as-cast Ti-48Al alloy, *J. Mater. Sci.* 42 (21) (2007) 9063–9069.

- [22] T. Liu, L. S. Luo, D. H. Zhang, L. Wang, X. Z. Li, R. R. Chen, Y. Q. Su, J. J. Guo, and H. Z. Fu, Comparison of microstructures and mechanical properties of as-cast and directionally solidified Ti-47Al-1W-0.5Si alloy, *Metallurg. Trans. A*, 682 (2016) 663–671.
- [23] F. Sun and F. H. S. Froes, Precipitation of Ti_5Si_3 phase in TiAl Alloys, *Mater. Sci. A* 328 (2002) 113–121.
- [24] S. Huang, E. L. Hall, The Effects of Cr Additions to Binary TiAl-Base Alloys, *Metallurg. Trans. A*, 22 (11) (1991) 2619-2627.
- [25] X. F. Ding, J. P. Lin, L. Q. Zhang, Y. Q. Su, H. L. Wang, and G. L. Chen, Lamellar orientation control in a Ti-46Al-5Nb alloy by directional solidification, *Scr. Mater.*, 65 (1) (2011) 61–64.
- [26] V. Haanappel, H. Clemens, M. Stroosnijder, The high temperature oxidation behaviour of high and low alloyed TiAl-based intermetallics, *Intermetallics* 10 (3) 92002) 293–305.
- [27] X.J. Zhao, H.Q. Ru, N. Zhang, X.Y. Wang, D.L. Chen, Corrosion of aluminum oxynitride based ceramics by molten steel, *Ceram. Inter.* 39 (2013) 3049–3054.
- [28] D. Pilone and F. Felli, Isothermal oxidation behaviour of TiAl-Cr-Nb-B alloys produced by induction melting, *Intermetallics*, 26 (2012) 36–39.
- [29] X. Du, S. Yao, X. Jin, Y. Long, B. Liang, W. Li, Photocatalytic properties of aluminum oxynitride (AlON), *Mater. Lett.* 161 (2015) 72–74.
- [30] A.S. Bolokang, D.E. Motaung, C.J. Arendse, T.F.G. Muller, Morphology and structural development of reduced anatase-TiO₂ by pure Ti powder upon annealing and nitridation: Synthesis of TiO_x and TiO_xN_y powders, *Materials Characterization* 100 (2015) 41–49.